MATERIALS SCIENCE

Bottom-up synthesis of two-dimensional carbon with vertically aligned ordered micropores for ultrafast nanofiltration

Chaehoon Kim[1], Dong-Yeun Koh[1], Yongjin Lee[2], Jihoon Choi[1], Hae Sung Cho[3], Minkee Choi[1]*

Two-dimensional (2D) carbon materials perforated with uniform micropores are considered ideal building blocks to fabricate advanced membranes for molecular separation and energy storage devices with high rate capabilities. However, creating high-density uniform micropores in 2D carbon using conventional perforation methods remains a formidable challenge. Here, we report a zeolite-templated bottom-up synthesis of ordered microporous 2D carbon. Through rational analysis of 255 zeolite structures, we find that the IWV zeolite having large 2D microporous channels and aluminosilicate compositions can serve as an ideal template for carbon replication. The resulting carbon is made of an extremely thin polyaromatic backbone and contains well-defined vertically aligned micropores (0.69 nm in diameter). Its areal pore density (0.70 nm^{-2}) is considerably greater than that of porous graphene (<0.05 nm^{-2}) prepared using top-down perforation methods. The isoporous membrane fabricated by assembling the exfoliated 2D carbon nanosheets exhibits outstanding permeance and molecular sieving properties in organic solvent nanofiltration.

INTRODUCTION

Two-dimensional (2D) carbon materials (e.g., graphene) with high thermochemical/mechanical stability and electroconductivity are important building blocks to fabricate membranes for molecular separation (*1*), electrochemical energy storage devices (e.g., Li batteries and supercapacitors) (*2*), and sensors (*3*). Perforation of uniform micropores in 2D carbon is essential to enhance surface area, create size-selective molecular transport pathways (*1*, *4*–*7*), and tune electronic bandgap (*8*, *9*). In conventional top-down perforation approaches, carbon atoms were locally ablated by focused-ion beam irradiation (*4*), ultraviolet-induced oxidative etching (*5*), ion bombardment combined with chemical oxidative etching (*6*), and oxygen plasma etching (*7*). Because of the stochastic interactions between the high-energy sources and carbon surface, technical hurdles exist in generating high-density micropores with narrow diameter distributions (the areal pore density is generally limited to less than 0.05 nm^{-2}) (*1*, *4*–*7*). In bottom-up synthesis approaches, specially designed polyaromatic bromide precursors were covalently linked by multistep cross-coupling reactions (*8*, *9*). The resulting carbon materials showed well-defined micropores but contained a large number of defect boundaries and pinholes due to incomplete cross-coupling between the organic precursors. Therefore, there is a great demand for the facile synthesis of 2D carbons having high-density uniform micropores.

It has been reported that carbon deposition within the 3D microporous channels of zeolites followed by zeolite dissolution can produce 3D carbon frameworks with ordered microporosity. The resulting ordered microporous carbons were often referred to as "zeolite-templated carbons (ZTCs)" (*10*–*16*). These materials can be synthesized when large-pore zeolites with ≥12-membered ring channels [e.g., FAU (*11*, *14*–*16*), EMT (*15*), and *BEA (*12*, *13*, *15*)] are used as templates (*10*). Narrower micropores generally prevent efficient connection of the internal carbon network, resulting in loss of structural order after zeolite dissolution. We believed that with rational selection of zeolite templates having 2D microporous channels, 2D carbon structures with ordered microporosity can also be created. After careful analysis of the 255 known zeolite structures, we found that 62 have 2D micropores and only 3 of them have large micropores. Notably, when further limited to the aluminosilicate composition providing sufficient acidity and thermal stability suitable for carbon deposition, only an IWV structure remained (fig. S1). In the present study, we report the bottom-up synthesis of ordered microporous 2D carbon using the IWV zeolite as a template. In addition, exfoliation of the 2D carbon and subsequent fabrication into an isoporous lamellar membrane for ultrafast nanofiltration are demonstrated.

RESULTS

Bottom-up synthesis of 2D carbon with vertically aligned ordered micropores

2DZTC was synthesized through carbon deposition on presynthesized IWV zeolite (Si/Al = 28) using 2% acetylene as a carbon source and subsequent zeolite etching with NaOH solution (see Materials and Methods). The IWV zeolite structure contains 2D microporous channels along the *b* and *c* axes (Fig. 1), which are constrained by the 14- and 12-membered rings, respectively (*17*). The channels are not interconnected along the *a* axis because they are separated by dense silicate layers. Therefore, the carbon frameworks grown inside the zeolite micropores are interconnected only within the *b*-*c* planes, which leads to the creation of microporous 2D carbon nanosheets after zeolite dissolution.

Scanning electron microscopy (SEM) revealed that 2DZTC had a sheet-like morphology with a lateral dimension of ~1 μm (Fig. 2A), which was similar to that of the initial IWV zeolite crystallites used

[1]Department of Chemical and Biomolecular Engineering, Korea Advanced Institute of Science and Technology (KAIST), Daejeon 34141, Republic of Korea. [2]Department of Chemistry and Chemical Engineering, Education and Research Center for Smart Energy and Materials, Inha University, Incheon 22212, Republic of Korea. [3]Department of Chemistry, Chung-Ang University, Seoul 06974, Republic of Korea.
*Corresponding author. Email: mkchoi@kaist.ac.kr

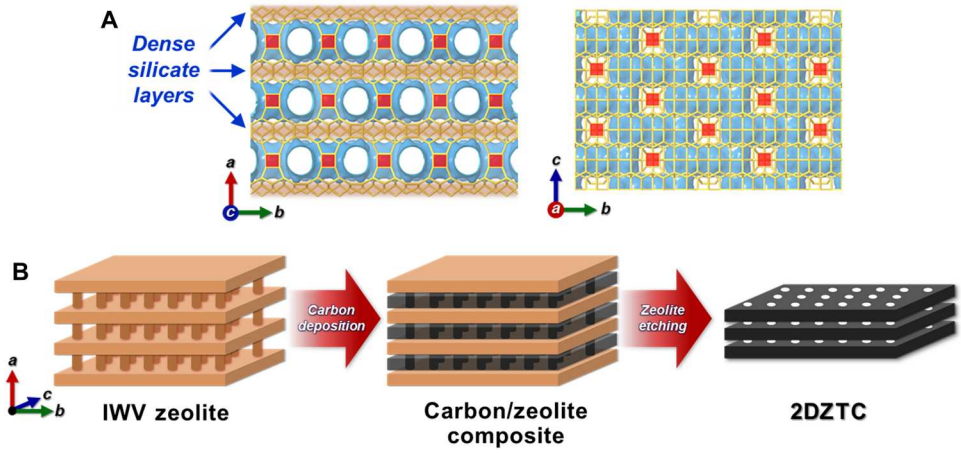

Fig. 1. Zeolite-templated bottom-up synthesis of 2DZTC. (**A**) Structural model of IWV zeolite. The 2D microporous channel surface and D4R pillars of the IWV zeolite are indicated by sky blue surface and red squares, respectively. (**B**) Synthesis scheme of 2DZTC using the IWV zeolite as a sacrificial template (a simplified zeolite model was used). The micropores of 2DZTC are created by the templating action of the D4R pillars of the zeolite.

as templates (Fig. 2B). Atomic force microscopy (AFM) images of the 2DZTC supported on a silicon wafer showed sheet-like particles with a thickness of ~30 nm (Fig. 2, C and D), indicating that multiple 2DZTC layers were stacked during the dissolution of the zeolite template. In the transmission electron microscopy (TEM) images, ordered micropores were clearly visible in domains with different thicknesses (Fig. 2E). This indicates that the micropores of the stacked 2DZTC layers are vertically aligned to maximize the π-π interactions between the carbon skeletons. In the TEM images, the micropores exhibited a mean pore size of 0.69 nm with a narrow diameter distribution (SD, 0.047 nm). This value was similar to the pore size (0.67 nm) calculated from the CO_2 adsorption isotherm at 273 K using nonlocal density functional theory (NLDFT; Fig. 2F). Notably, the areal pore density is calculated to be 0.70 nm^{-2} (fig. S2), which is an order of magnitude greater than porous graphene prepared by conventional top-down perforation methods (<0.05 nm^{-2}) (*4*–*7*).

In x-ray diffraction (XRD), 2DZTC exhibited a sharp peak at 2θ = 7.2° (*d*-spacing = 1.23 nm) due to the ordered arrangement of micropores (Fig. 2G). This peak position is consistent with that of the 020 reflection of the IWV zeolite (fig. S3) related to the distance between the double-4-ring (D4R) units of the IWV zeolite structure in the *b* direction. This indicates that the ordered micropores of 2DZTC were created by replicating the D4R-containing pillars of the IWV zeolite (D4R units are indicated as red squares in Fig. 1). An additional XRD peak at 2θ = 25.1° could be attributed to the stacking of 2DZTC layers due to strong π-π interactions. The interlayer spacing was calculated to be 0.356 nm, which was slightly larger than that of graphite (0.335 nm) (*18*). The Raman spectrum of 2DZTC (Fig. 2H) showed a pronounced D band at 1370 cm^{-1} in addition to the G band at 1580 cm^{-1}, which was attributed to the abundant carbon edge sites around the micropores (*19*, *20*). Similar Raman spectra were observed for perforated graphene (*6*–*8*), whereas defect-free graphene showed a very weak D band (*20*).

To obtain deeper insight into the atomic structure of 2DZTC, theoretical modeling was carried out by combining Metropolis Monte Carlo (MMC) and density functional theory (DFT) calculations (Fig. 2I; see Materials and Methods). The atomic model was prepared to fully reflect the following experimental results (table S1). Thermogravimetric analysis showed that 0.18 g of carbon was deposited per gram of the zeolite template. Elemental analysis showed that 2DZTC contained a large amount of H (H/C ratio of 0.32) and O (O/C ratio of 0.064), indicating the presence of abundant H- and O-terminated carbon edges sites. C 1s x-ray photoelectron spectroscopy (XPS) showed that 2DZTC consists of solely sp^2-hybridized carbons (fig. S4A). O 1s XPS indicated that 2DZTC has the C—O:O═C—O:C═O functional group ratio of 0.31:0.46:0.23 (fig. S4B). The simulated atomic structure (Fig. 2I) showed that 2DZTC consists of an extremely thin sp^2-hybridized polyaromatic backbone composed of not only carbon hexagons but also pentagons and heptagons to achieve optimal framework curvature that fits well within the zeolite microporous channels. The XRD pattern simulated using the 2DZTC model was also consistent with the experimental XRD pattern (fig. S5). In addition, the effective pore diameter of the model was calculated to be 0.67 nm, which is in exact agreement with that determined by CO_2 adsorption.

Fabrication of isoporous lamellar membrane

Graphene and graphene oxide (GO) have been extensively used to fabricate advanced membranes (*1*). Because of its atomic thickness, monolayer graphene is considered the ultimate membrane that can maximize permeance (*1*). Since graphene is impermeable to any molecules or ions (*21*), in-plane pores must be created by top-down perforation methods (*4*–*7*). However, as mentioned earlier, there are still technical hurdles in creating uniform micropores at high areal densities (*1*). Alternatively, GO can be assembled into lamellar membranes in which interlayer channels provide molecular transport pathways (*22*–*27*). Because of its high solvent dispersibility, GO is solution processable and suitable for large-scale membrane production (*1*, *25*). However, these membranes are relatively disadvantageous in achieving high permeation fluxes because molecules or ions must pass through tortuous pathways between the stacked nonporous GO sheets (*1*, *27*). Recently, it has been proposed that the advantages of two membrane systems can be synergistically combined by stacking microporous 2D carbon into lamellar membranes (*28*). To realize this concept, the synthesis of

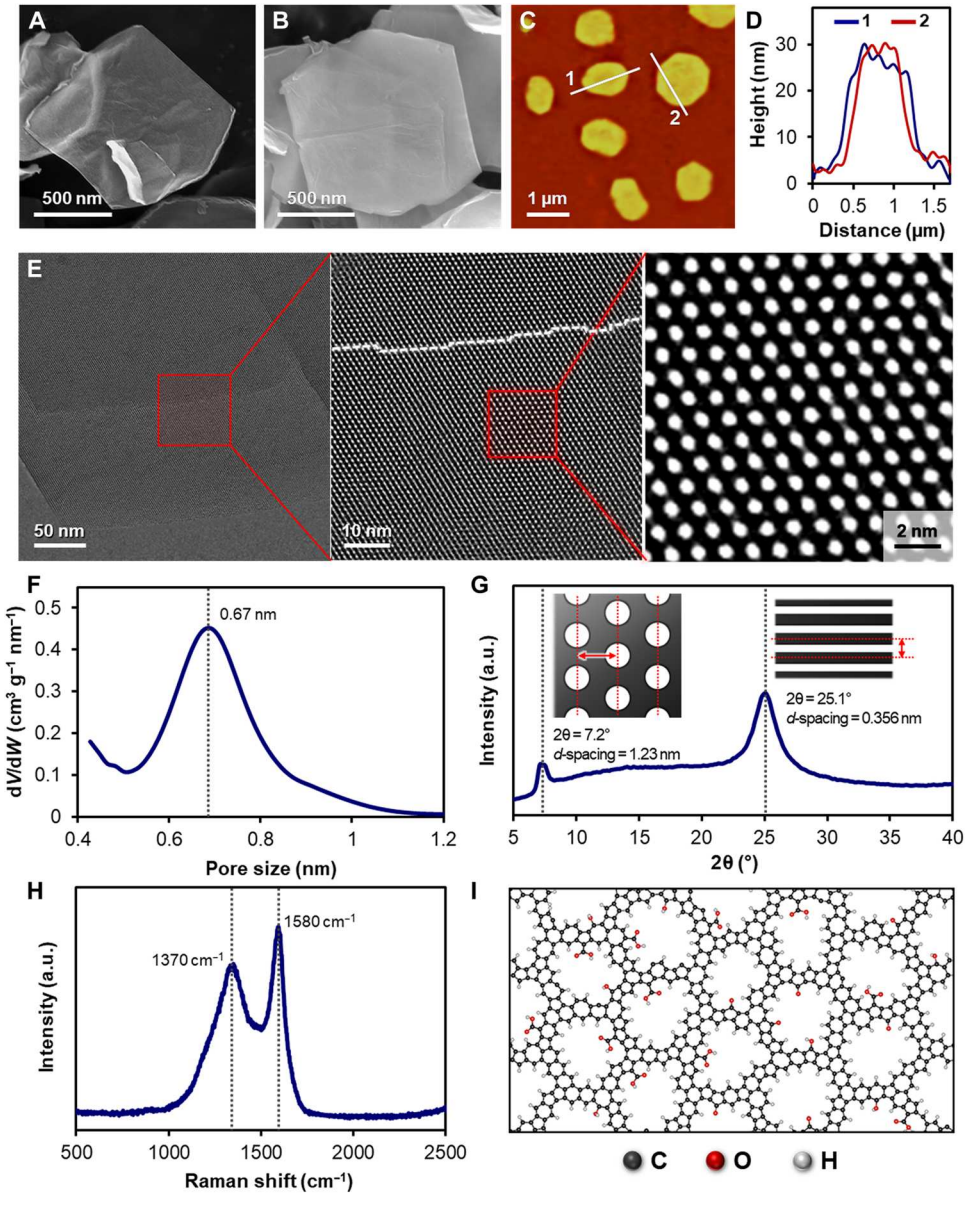

Fig. 2. Structural characterization of 2DZTC. (**A** and **B**) SEM images of 2DZTC particles (A) and IWV zeolite crystallites (B). (**C**) AFM image of the 2DZTC particles loaded on a silicon wafer. (**D**) Height profiles of lines 1 and 2 in (C). (**E** to **H**) TEM images (E), nonlocal density functional theory (NLDFT) pore size distribution calculated from CO_2 adsorption at 273 K (F), x-ray diffraction pattern (λ = 1.5406 Å) (G), and Raman spectrum (H) of 2DZTC. White dashed line in (E) indicates step edges. (**I**) Atomic structure of 2DZTC simulated by combining Metropolis Monte Carlo and DFT calculations. a.u., arbitrary units.

dispersible 2D carbon with high-density uniform micropores must be preceded. We expected that 2DZTC can serve as an ideal material platform for preparing such membranes.

To fabricate a pinhole-free lamellar membrane, 2DZTC must be exfoliated into solvent-dispersible single- or few-layer carbon nanosheets and then reassembled into an interlocked multilayer structure. However, when the zeolite template was removed, the as-synthesized 2DZTC nanosheets were immediately stacked into multilayered aggregates that were difficult to exfoliate because of very strong π-π interactions. To overcome this problem, the accessible carbon surface within zeolite micropores was gently oxidized using a diluted $KMnO_4$ solution, and then zeolite etching was performed with NaOH solution. The partially oxidized 2DZTC (*o*-2DZTC) exhibited a slightly enlarged interlayer spacing in XRD (0.397 nm; fig. S6) due to the increased amount of oxygen functional groups [O content, 13.4 weight % (wt%)] and weakened interlayer π-π interactions. Exfoliation of the *o*-2DZTC was performed by applying high shear stress using a rotor-stator homogenizer. The exfoliated *o*-2DZTC was solvent-exchanged with *N*-methyl pyrrolidone (NMP) and centrifuged twice at 9000 rpm to remove unexfoliated particles (fig. S7). The resultant *o*-2DZTC solution could be stable for 48 hours without precipitation (Fig. 3A). AFM images of the *o*-2DZTC showed sheet-like particles with a thickness of less than 1 nm, indicating that most of the *o*-2DZTC

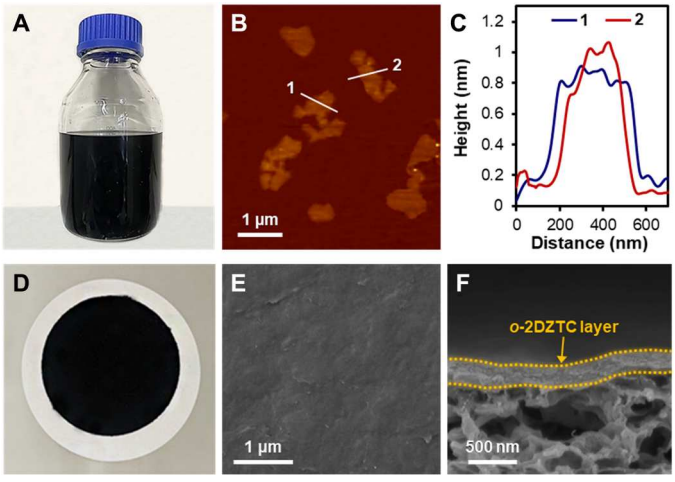

Fig. 3. Preparation of *o*-2DZTC solution and membrane fabrication. (**A**) Photograph of the *N*-methyl pyrrolidone solution containing exfoliated oxidized 2DZTC (*o*-2DZTC). (**B**) AFM image of the *o*-2DZTC particles loaded on a silicon wafer. (**C**) Height profiles of lines 1 and 2 in (B). (**D**) Photograph of the *o*-2DZTC membrane fabricated by filtration of the *o*-2DZTC solution through a porous nylon support. (**E** and **F**) SEM images of the *o*-2DZTC membrane: top surface image (E) and cross-sectional image (F).

sheets consisted of a single or few carbon layers (Fig. 3, B and C). In the TEM images of the exfoliated *o*-2DZTC, the ordered micropore array was still clearly visible (fig. S8), indicating that the gentle oxidation and exfoliation steps did not damage the structural order of 2DZTC.

Membrane fabrication was carried out by pressurized filtration of the *o*-2DZTC NMP solution through a commercial nylon membrane with a pore size of 0.1 μm. The nylon membrane was chosen as a support because of its excellent stability in various organic solvents, including NMP (fig. S9). The resultant membrane had a uniform surface with a smooth finish and a high degree of mechanical flexibility (Fig. 3D and fig. S10). SEM investigation of the membrane surface indicated the absence of visible defects or pinholes (Fig. 3E). The cross-sectional SEM image of the membrane revealed a selective layer thickness of 300 nm (Fig. 3F). The TEM image of the scratched *o*-2DZTC selective layer showed the presence of vertically aligned micropores with distinct FFT patterns corresponding to the ordered micropore array (fig. S11).

Evaluation of membrane performances

The permeance of pure water and various organic solvents (Fig. 4A) was evaluated using a laboratory-made cross-flow filtration setup. The permeance was inversely proportional to the liquid viscosity. The product of permeance and viscosity was nearly constant regardless of the Hansen solubility parameter (fig. S12), indicating that the solvent transport followed the pore flow model without any specific interaction between the solvent and membrane surface (*26*, *29*). When the thickness of the selective layer was adjusted, solvent permeance and the layer thickness showed an inverse relationship (fig. S13), which was in good agreement with the transport model. This result also indicates that the vertically aligned micropores of *o*-2DZTC are not blocked during their multilayer stacking into membranes.

Notably, the *o*-2DZTC membrane exhibited two orders of magnitude larger solvent permeance than the GO membrane of the same thickness (300 nm; fig. S14). In GO membranes, molecules are known to diffuse through tortuous pathways between stacked GO layers (interlayer channels, Fig. 4B) (*1*, *27*). It has been reported that the interlayer channel size of GO membranes can vary in the range of 0.5 to 1.0 nm [calculated assuming that the thickness of individual GO sheets is 0.335 nm, equal to that of graphene (*22*)] depending on solvent type due to swelling (*26*). Conversely, the *o*-2DZTC membrane exhibited a substantially smaller interlayer channel size of 0.062 nm, and it was not affected by solvent type (fig. S15). These results indicated stronger π-π interactions between *o*-2DZTC layers than between GO layers, which can be attributed to the considerably lower oxygen content of the former (13.4 wt%) than that of the latter (53.8 wt%). Because the interlayer channel size of the *o*-2DZTC membrane (0.062 nm) is too small for molecular diffusion, its large liquid permeance can be attributed to the rapid molecular transport through the high-density micropores (Fig. 4B). To better understand the molecular transport pathways, *o*-2DZTC and GO membranes were thermally reduced at 423 K under vacuum. This treatment resulted in a substantial reduction in oxygen content (from 13.4 to 4.9 wt% for *o*-2DZTC and from 53.8 to 7.51 wt% for GO) and narrowing of interlayer channels (the channel size decreased below 0.1 nm for both materials; fig. S16). The thermally reduced GO membrane exhibited dramatically reduced solvent permeance compared to the pristine one (>74% decrease; Fig. 4C), confirming that the interlayer channel is the major molecular transport pathway of the GO membrane. In contrast, the thermally reduced *o*-2DZTC membrane showed a minor decrease in permeance (<17% decrease; Fig. 4D), indicating that the ordered micropores are the major pathways for molecular transport (Fig. 4B).

The nanofiltration performance of the *o*-2DZTC membrane was evaluated using methanolic solutions containing styrene oligomers with various molecular weights (MWs). The membrane showed precise molecular sieving properties in the MW range of 162 to 370 g mol^{-1} (Fig. 4E). MW retention onset (MW at 10% rejection) and MW cutoff (MWCO, MW at 90% rejection) values of the membrane were determined to be 186 and 344 g mol^{-1}, respectively. Using the rejection data and log-normal probability density function, the effective pore size of the *o*-2DZTC membrane was calculated to be 0.69 nm (fig. S17). This is in excellent agreement with the pore size of *o*-2DZTC (0.66 nm) determined using CO_2 adsorption (fig. S18). The nanofiltration performance of the *o*-2DZTC membrane was compared with that of other nanofiltration membranes reported in the literature (Fig. 4F) (*29*–*47*). The *o*-2DZTC membrane simultaneously exhibited very high methanol permeance and precise molecular separation with an MWCO of 344 g mol^{-1}, surpassing the upper bound of previously reported polymer–, metal organic framework–, and covalent organic framework–based membranes.

To evaluate long-term membrane stability, nanofiltration performance was measured for 24 hours under continuous cross-flow operation. The *o*-2DZTC membrane exhibited a stable methanol permeance of ~890 liters m^{-2} $hour^{-1}$ bar^{-1} and styrene oligomer rejection (MWCO of ~350 g mol^{-1}) (fig. S19), indicating robust membrane integrity under hydrodynamic shear stress. The membrane stability was additionally investigated by immersing it in various solvents (acetonitrile, tetrahydrofuran, toluene,

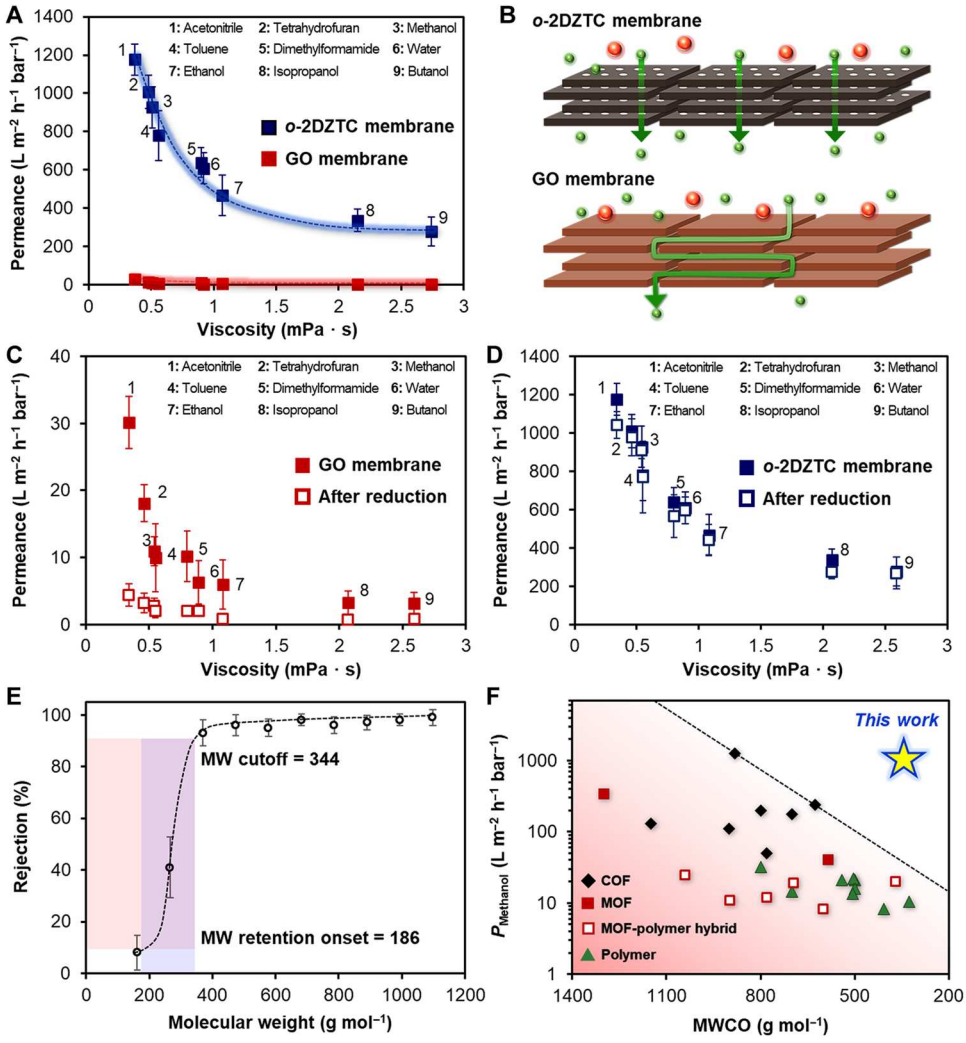

Fig. 4. Nanofiltration properties of the *o*-2DZTC membrane. (**A**) Permeance of pure water and organic solvents as a function of viscosity over the *o*-2DZTC and GO membranes having selective layers of equal thickness (300 nm). (**B**) Schematic representation of molecular transport pathways in *o*-2DZTC and GO membranes. Solute (styrene oligomer) and solvent molecules are represented as red and green spheres, respectively. (**C** and **D**) Permeance of various solvents through the GO membranes (C) and *o*-2DZTC membranes (D) before and after thermal reduction at 423 K. (**E**) Nanofiltration performance of the *o*-2DZTC membrane for styrene oligomers dissolved in methanol. (**F**) MWCO-versus-permeance (methanol) plot of various nanofiltration membranes.

dimethylformamide, and water) and acidic/basic aqueous solutions (pH 2 and 13) for 24 hours. After all treatments, the membrane integrity remained intact (fig. S20), and nanofiltration properties were not altered (fig. S21). Such high stability is consistent with earlier XRD analysis (fig. S15), showing that the stacked *o*-2DZTC layers do not swell in various solvents due to strong π-π interactions.

DISCUSSION

We have demonstrated that ordered microporous 2D carbon can be synthesized by carbon replication of the IWV zeolite as a template. The resulting carbon is built with an extremely thin polyaromatic backbone and contains well-defined vertically aligned micropores (0.69 nm in diameter). Its areal pore density (0.70 nm^{-2}) is noticeably greater than that of porous graphene (<0.05 nm^{-2}) prepared using top-down perforation methods. This carbon could be gently oxidized, exfoliated to prepare a stable solution, and reassembled into an isoporous lamellar membrane for ultrafast nanofiltration. It is anticipated that various functional groups can be additionally introduced at the abundant edge sites around the carbon micropores (*10*) to precisely tune the molecular separation properties. Whereas conventional ZTCs with 3D frameworks are highly promising for gas adsorptions (*10*, *13*, *14*), the present 2DZTC with vertically aligned micropores and interlayer stackings can be used for the fabrication of advanced membranes and electrochemical energy storage devices with high rate capabilities.

MATERIALS AND METHODS

Synthesis of organic structure–directing agent

IWV zeolite was synthesized using diquaternary imidazolium as an organic structure–directing agent (OSDA) (*48*). For the synthesis of OSDA, 24.8 g of 1,2,4,5-tetramethylimidazole (>98.0%, TCI) and 23.0 g of 1,5-dibromopentane (>97.0%; Sigma-Aldrich) were

dissolved in 100 ml of methanol (>99.9%; Samchun Chemicals) and refluxed at 343 K overnight. Then, methanol was removed using a rotary evaporator, and the resulting product was recrystallized using 300 ml of diethyl ether (>99.0%; Samchun Chemicals). The precipitate was filtered, washed thoroughly with diethyl ether, and dried overnight at 323 K under vacuum. The resulting OSDA (Br^- form) was dissolved in deionized water and converted to OH^- form using Trilite MA-12OH ion-exchange resin (Samyang). The final concentration of OH^--form OSDA was determined using a Mettler-Toledo DL22 autotitrator with 0.01 M HCl as titrant.

Synthesis of IWV zeolite

IWV zeolite was synthesized as reported previously (*48*) with some modifications. After dissolving 2.30 g of NaOH (>97.0%; Junsei) in 232 g of deionized water, 190 g of an aqueous OSDA solution (34 wt %, OH^- form) was added. Under vigorous stirring, 60 g of ultrastable Y zeolite (CBV760, Si/Al = 30; Zeolyst) and 10 g of colloidal silica (Ludox AS-30, Sigma-Aldrich) were added to the solution. The mixture was hydrothermally crystallized at 458 K in a Teflon-lined autoclave under tumbling (30 rpm) for 12 days. The solid product was filtered and thoroughly washed with deionized water until the pH of the filtrate was neutral. The sample was dried at 373 K for 6 hours and calcined at 823 K (ramp, 2 K min^{-1}) for 6 hours in dry air (200 cm^3 min^{-1}) to remove OSDA.

Synthesis of 2DZTC

For the synthesis of 2DZTC, 5.0 g of IWV zeolite was placed in a quartz plug-flow reactor (inner diameter, 5.5 cm) and heated to 823 K (ramp, 2 K min^{-1}) under Ar flow (200 cm^3 min^{-1}). After stabilizing the temperature for 30 min, 2% acetylene/Ar was flowed (200 cm^3 min^{-1}) for 12 hours. Then, the temperature was increased to 1273 K (ramp, 2 K min^{-1}) under Ar flow (200 cm^3 min^{-1}) and held for 2 hours. The chemical vapor deposition of acetylene at 823 K and the thermal treatment at 1273 K were repeated once again. To remove the zeolite template, 5.0 g of the carbon/zeolite composite was treated with 100 ml of 50 wt% NaOH aqueous solution at 373 K for 1 day under magnetic stirring in a polypropylene bottle. The resultant carbon was filtered, thoroughly rinsed with deionized water, and dried at 373 K.

Synthesis and exfoliation of *o*-2DZTC

For the synthesis of *o*-2DZTC, 1.5 g of the carbon/zeolite composite was dispersed in 100 ml of deionized water. After bath sonication for 30 min, 0.5 g of $KMnO_4$ (>99.5%; Junsei) was slowly added under vigorous stirring at room temperature and heated at 333 K for 12 hours. After the oxidation reaction, the carbon/zeolite composite was collected by centrifugation at 9000 rpm. Washing with deionized water and collecting the sample by centrifugation were repeated three times. The solid product was treated with 30 ml of 50 wt% NaOH aqueous solution at 373 K for 1 day under magnetic stirring in a polypropylene bottle. For the exfoliation of *o*-2DZTC, 30 ml of the resultant solution was treated with a rotor-stator homogenizer (HG-15A, DAIHAN Scientific) at 16,000 rpm for 40 min. After diluting the resulting thick solution with 170 ml of deionized water, the solid carbon product was collected by centrifugation at 9000 rpm. Washing with deionized water and collecting the sample by centrifugation were repeated two times. The collected *o*-2DZTC was redispersed in 2 liters of NMP (>99.0%; Junsei) and sonicated at room temperature for 6 hours. The solution was centrifuged twice at 9000 rpm to remove particles that had not been exfoliated (e.g., intergrown particles; fig. S7). To determine the concentration of exfoliated *o*-2DZTC sheets in the resulting solution, 200 ml of the solution was filtered on a preweighed anodized aluminum oxide (AAO) support with an average pore size of 20 nm (Whatman). The AAO was dried under vacuum at 333 K for 12 hours, and the weight change after filtration was analyzed to determine the initial concentration of *o*-2DZTC in the NMP solution. Typically, the concentration of exfoliated *o*-2DZTC in the NMP solution was determined to be 32 ± 5 mg $liter^{-1}$.

Fabrication of *o*-2DZTC lamellar membrane

Before membrane fabrication, the aforementioned *o*-2DZTC NMP solution was further diluted with NMP to reduce the *o*-2DZTC concentration to 0.2 mg $liter^{-1}$. After bath sonication for 1 hour at room temperature, 1.5 liters of the solution was filtered on a commercial nylon support (GVS; mean pore size, 0.1 μm) at a transmembrane pressure of 0.2 bar using a pressurized filtration setup. After filtration, the *o*-2DZTC membrane was dried subsequently under vacuum at 303 K for 12 hours and at 333 K for 6 hours.

Fabrication of GO lamellar membrane

GO was synthesized using a modified Hummers′ method. While stirring in an ice bath, 1.0 g of synthetic graphite (Sigma-Aldrich) was dispersed in 100 ml of concentrated sulfuric acid (>97%; Samchun Chemicals). Then, 3.0 g of $KMnO_4$ was slowly added to the solution over a period of 30 min. After stirring in the ice bath for 2 hours, the mixture was heated for 6 hours at 323 K. After the reaction, 200 ml of ice-cooled deionized water was added carefully, and the mixture was stirred for 30 min in an ice bath. After adding 10 ml of hydrogen peroxide (30%; Samchun Chemicals), the mixture was stirred for 30 min and centrifuged at 9000 rpm for 30 min to precipitate GO cake. The GO cake was washed with deionized water multiple times until the pH of the supernatant reached 7. The GO cake was dispersed in 100 ml of deionized water and sonicated for 3 hours. The solution was centrifuged twice at 9000 rpm for 30 min to remove species that had not been exfoliated. The concentration of GO in the aqueous solution was determined in a similar manner to the *o*-2DZTC NMP solution. Typically, the concentration of GO was determined to be 1.0 ± 0.1 g $liter^{-1}$.

For the preparation of GO lamellar membrane, the GO solution was further diluted with deionized water to prepare a solution containing 1.0 mg $liter^{-1}$ of GO. Then, 300 ml of the solution was filtered through a commercial nylon support (GVS; mean pore size, 0.1 μm) at a transmembrane pressure of 0.2 bar using a pressurized filtration setup. After filtration, the GO membrane was dried under vacuum at 303 K for 12 hours and at 333 K for 6 hours.

Computational modeling of 2DZTC structure

We generated a fully relaxed 2DZTC structure by combining continuous random network model–based MMC (CRN-MMC) simulations, DFT calculations, and molecular simulations. The initial configuration of 2DZTC was prepared by locating carbon atoms inside the IWV zeolite micropores with the number of carbon atoms determined according to the carbon deposition amount measured in the experiment. Next, we relaxed the carbon structure using our in-house code performing CRN-MMC simulations; more details regarding CRN-MMC simulations can be found in (*49*).

After the CRN-MMC simulation, the zeolite template was removed, and undercoordinated carbon atoms were terminated with hydrogen atoms. Then, we further optimized the zeolite-free structure by DFT calculations. Our DFT calculations were performed within the generalized gradient approximation of Perdew, Burke, and Ernzerhof (*50*) using the Vienna ab initio simulation package (*51*). We used a plane-wave basis set and projector-augmented wave pseudopotentials(*52*, *53*). A (2 × 2 × 2) k-point grid in the Monkhorst-Pack grid scheme was used for the Brillouin zone sampling. We set the convergence criterion of wave function energy as 10^{-4} eV. Atomic positions and unit cell volume were optimized until all forces were smaller than 0.01 eV/Å. Cell parameters of DFT-optimized 2DZTC are α = β = γ = 90°; a = 3.491 Å, b = 25.183 Å, and c = 13.801 Å.

To generate the 2DZTC structure with oxygen functional groups, we first expanded the unit cell of 2DZTC by 3×3 times in both in-plane directions (b and c). The resultant dimensions of the expanded 2DMC model were 3.491 by 75.551 by 41.402 $Å^3$. Then, according to the ratio of functional groups experimentally determined, we manually generated functional groups at the edges of 2DZTC. Next, we performed geometry optimization using the ReaxFF reactive force field potential (*54*). The effective pore diameter of 2DZTC was estimated as the largest free sphere along the free path (the out-of-place direction of 2DZTC) using the open-source software Zeo++ (*55*).

Materials characterizations

Elemental analysis (C, H, and O) was performed using a FLASH 2000 analyzer (Thermo Fisher Scientific). Before elemental analysis, all samples were dried under vacuum at 323 K for 12 hours. XRD patterns were recorded using a Smartlab x-ray diffractometer (RIGAKU) equipped with a CuKα radiation source (λ = 1.5406 Å, 40 kV, 300 mA). C 1s and O 1s XPS measurements were carried out on a Sigma Probe instrument (Thermo Fisher Scientific VG) equipped with a microfocused monochromator x-ray source. CO_2 adsorption isotherms were measured with an ASAP 2020 (Micromeritics) at 273 K. Before the measurement, all samples were degassed under vacuum at 473 K for 12 hours. The pore size distributions were calculated using the NLDFT method. TEM images were taken using a field emission TEM (JEM-2100F HR) operated at 200 kV after mounting the samples on a lacey carbon grid (LC300-Cu). SEM images were collected using an SU8230 (HITACHI) operating at 3 kV without metal coating. Raman spectra were recorded using a LabRAM ARAMIS with an Ar ion laser (514 nm). AFM images were collected in a tapping mode in air using a Multimode 8 (Bruker) equipped with a silicon cantilever and an RTESPA-150 tip. Before AFM investigation, a fresh silicon wafer was coated with a drop of diluted *o*-2DZTC NMP solution (0.01 mg ml^{-1}) and then dried under vacuum at 298 K for 12 hours.

Evaluation of membrane performance

All nanofiltration experiments were carried out using a continuous cross-flow setup, where the membrane is clamped and sealed with silicone O-ring. The experiments were conducted under a cross-flow rate of 50 liters $hour^{-1}$ and a transmembrane pressure of 1 bar at room temperature. Solvent permeance was calculated by measuring the weight change of the solvents collected in the permeate side after 3 hours of stabilization. Permeance, P (liters m^{-2} $hour^{-1}$ bar^{-1}), was calculated using Eq. 1

$$P = \frac{V}{At\Delta p} \tag{1}$$

where V is the volume of permeate collected (liters), A is the effective membrane area (m^2), t is the permeation time (hours), and Δp is the trans-membrane pressure (bar). The effective membrane area was determined to be 5.11×10^{-4} m^2.

The solute rejection properties of the *o*-2DZTC membrane were investigated using standard methanol solutions containing styrene oligomers with different MWs. The standard solutions were prepared by dissolving 0.1 g of PSS-PS162 (nominal MW, 162; polydispersity index (PDI), 1.00; Polymer Standard Service), 0.1 g of PSS-PS266 (nominal MW, 266; PDI, 1.00; Polymer Standard Service), 0.1 g of PSS-PS370 (nominal MW, 370; PDI, 1.00; Polymer Standard Service), and 0.5 g of PSS-PS750 (nominal MW, 750; PDI, 1.09; Polymer Standard Service) in 1 liter of methanol [high-performance liquid chromatography (HPLC) grade, Samchun Chemicals]. Styrene oligomer concentration in the permeate was analyzed using an Agilent HPLC system equipped with an ultraviolet-visible detector set at a wavelength of 264 nm. Separation was accomplished using a reverse-phase column (ACE 5-C18-100). A mobile phase composed of 35 vol% water (HPLC grade, Daejung Chemicals) and 65 vol% tetrahydrofuran (HPLC grade, Samchun Chemicals) was used with 0.1 vol% trifluoroacetic acid (HPLC grade, Alfa Aesar). Rejection rates of the styrene oligomers were measured using the permeate solution collected after 3 hours of stabilization. The rejection rate, R_i (%), was calculated by Eq. 2

$$R_i = \left(1 - \frac{C_{p,i}}{C_{f,i}}\right) \times 100\% \tag{2}$$

where $C_{p,i}$ and $C_{f,i}$ are the concentrations of each styrene oligomer in the permeate and feed solutions, respectively. All experiments were carried out thrice to ensure reproducibility.

Theoretical analysis of rejection data

From the styrene oligomer rejection data, the effective pore size distribution of *o*-2DZTC membrane was estimated using the log-normal distribution functions (*56*, *57*). The solute rejection, R, can be expressed by a log-normal probability function of the solute size, as described in Eq. 3

$$R = \mathrm{erf}(y) = \frac{1}{\sqrt{2\pi}}\int_{-\infty}^{y} e^{-\left(\frac{u^2}{2}\right)} du, \text{where } y = \frac{\ln r_s - \ln r_s^*}{\ln \sigma_g} \tag{3}$$

where r_s is the solute radius, r_s^* is the geometric mean radius of solute at R = 50%, and σ_g is the geometric SD about r_s^*, defined as the ratio of r_s at R = 84.13 and 50%. When the solute rejection is plotted against the solute radius on the log-normal probability coordinates, a straight line is yielded as follows

$$F(R) = A_0 + A_1(\ln r_s) \tag{4}$$

where A_0 and A_1 are the intercept and the slope, respectively. From this log-normal plot, r_s^* and σ_g can be determined. By ignoring the dependence of solute separation on the steric and hydrodynamic interactions between the solute and pore surfaces (*58*), the mean pore radius (r_p^*) and the corresponding geometric SD (σ_p) can be assumed to be the same with r_s^* and σ_g, respectively. Therefore, the pore size distribution of the membrane can be expressed as the

following probability density function

$$\frac{dR(r_p)}{dr_p} = \frac{1}{r_p \ln \sigma_p \sqrt{2\pi}} \exp\left[-\frac{(\ln r_p - \ln r_p^*)^2}{2(\ln \sigma_p)^2}\right] \quad (5)$$

where r_p is the pore radius of the membrane.

The size of styrene oligomer dissolved in methanol was calculated as the equivalent spherical radius (also called Einstein-Stokes radius) using Eq. 6

$$r_s = \frac{k_B T}{6\pi\mu_0 D_\infty} \quad (6)$$

where k_B is the Boltzmann constant (1.38×10^{-23} J K^{-1}), T is the temperature (K), μ_0 is the viscosity of bulk solution (cP), and D_∞ is the diffusion coefficients of the solute in the bulk solvent (cm^2 s^{-1}). D_∞ can be calculated using the Wilke-Chang correlation, as described in Eq. 7 (*59*)

$$D_\infty = 7.4 \times 10^{-8} \frac{T\sqrt{\alpha_{sv} M_{sv}}}{\mu_0 (\alpha_s V_s)^{0.6}} \quad (7)$$

where M_{sv} is the MW of solvent (g mol^{-1}), V_s is the solute molar volume at a normal boiling point (cm^3 mol^{-1}), and α_s and α_{sv} are the dimensionless association coefficients of the solute and solvent, respectively. The dimensionless association coefficient of the solvent was used according to Miyabe and Isogai (*60*), whereas the solute was presumed to be nonassociating ($\alpha_s = 1$) (*60*). The solute molar volumes were estimated using the group contribution methods (*61*).

Supplementary Materials

This PDF file includes:

Figs. S1 to S21

Table S1

REFERENCES AND NOTES

1. G. Liu, W. Jin, N. Xu, Graphene-based membranes. *Chem. Soc. Rev.* **44**, 5016–5030 (2015).
2. R. Raccichini, A. Varzi, S. Passerini, B. Scrosati, The role of graphene for electrochemical energy storage. *Nat. Mater.* **14**, 271–279 (2015).
3. Y. Liu, X. Dong, P. Chen, Biological and chemical sensors based on graphene materials. *Chem. Soc. Rev.* **41**, 2283–2307 (2012).
4. K. Celebi, J. Buchheim, R. M. Wyss, A. Droudian, P. Gasser, I. Shorubalko, J.-I. Kye, C. Lee, H. G. Park, Ultimate permeation across atomically thin porous graphene. *Science* **344**, 289–292 (2014).
5. S. P. Koenig, L. Wang, J. Pellegrino, J. S. Bunch, Selective molecular sieving through porous graphene. *Nat. Nanotechnol.* **7**, 728–732 (2012).
6. S. C. O'Hern, M. S. H. Boutilier, J.-C. Idrobo, Y. Song, J. Kong, T. Laoui, M. Atieh, R. Karnik, Selective ion transport through tunable subnanometer pores in single-layer graphene membranes. *Nano Lett.* **14**, 1234–1241 (2014).
7. S. P. Surwade, S. N. Smirnov, I. V. Vlassiouk, R. R. Unocic, G. M. Veith, S. Dai, S. M. Mahurin, Water desalination using nanoporous single-layer graphene. *Nat. Nanotechnol.* **10**, 459–464 (2015).
8. C. Moreno, M. Vilas-Varela, B. Kretz, A. Garcia-Lekue, M. V. Costache, M. Paradinas, M. Panighel, G. Ceballos, S. O. Valenzuela, D. Peña, A. Mugarza, Bottom-up synthesis of multifunctional nanoporous graphene. *Science* **360**, 199–203 (2018).
9. P. H. Jacobse, R. D. McCurdy, J. Jiang, D. J. Rizzo, G. Veber, P. Butler, R. Zuzak, S. G. Louie, F. R. Fischer, M. F. Crommie, Bottom-up assembly of nanoporous graphene with emergent electronic states. *J. Am. Chem. Soc.* **142**, 13507–13514 (2020).
10. H. Nishihara, T. Kyotani, Zeolite-templated carbons—Three-dimensional microporous graphene frameworks. *Chem. Commun.* **54**, 5648–5673 (2018).
11. Z. Ma, T. Kyotani, A. Tomita, Preparation of a high surface area microporous carbon having the structural regularity of Y zeolite. *Chem. Commun.* , 2365–2366 (2000).
12. T. Kyotani, Z. Ma, A. Tomita, Template synthesis of novel porous carbons using various types of zeolites. *Carbon* **41**, 1451–1459 (2003).
13. Z. Yang, Y. Xia, R. Mokaya, Enhanced hydrogen storage capacity of high surface area zeolite-like carbon materials. *J. Am. Chem. Soc.* **129**, 1673–1679 (2007).
14. N. P. Stadie, M. Murialdo, C. C. Ahn, B. Fultz, Anomalous isosteric enthalpy of adsorption of methane on zeolite-templated carbon. *J. Am. Chem. Soc.* **135**, 990–993 (2013).
15. K. Kim, T. Lee, Y. Kwon, Y. Seo, J. Song, J. K. Park, H. Lee, J. Y. Park, H. Ihee, S. J. Cho, R. Ryoo, Lanthanum-catalysed synthesis of microporous 3D graphene-like carbons in a zeolite template. *Nature* **535**, 131–135 (2016).
16. H. Nishihara, H. Fujimoto, H. Itoi, K. Nomura, H. Tanaka, M. T. Miyahara, P. A. Bonnaud, R. Miura, A. Suzuki, N. Miyamoto, N. Hatakeyama, A. Miyamoto, K. Ikeda, T. Otomo, T. Kyotani, Graphene-based ordered framework with a diverse range of carbon polygons formed in zeolite nanochannels. *Carbon* **129**, 854–862 (2018).
17. D. L. Dorset, G. J. Kennedy, K. G. Strohmaier, M. J. Diaz-Cabañas, F. Rey, A. Corma, P-derived organic cations as structure-directing agents: Synthesis of a high-silica zeolite (ITQ-27) with a two-dimensional 12-ring channel system. *J. Am. Chem. Soc.* **128**, 8862–8867 (2006).
18. S. Park, R. S. Ruoff, Chemical methods for the production of graphenes. *Nat. Nanotechnol.* **4**, 217–224 (2009).
19. G. Katagiri, H. Ishida, A. Ishitani, Raman spectra of graphite edge planes. *Carbon* **26**, 565–571 (1988).
20. M. S. Dresselhaus, A. Jorio, A. G. Souza Filho, R. Saito, Defect characterization in graphene and carbon nanotubes using Raman spectroscopy. *Philos. Trans. R. Soc. A* **368**, 5355–5377 (2010).
21. J. Scott Bunch, S. S. Verbridge, J. S. Alden, A. M. van der Zande, J. M. Parpia, H. G. Craighead, P. L. McEuen, Impermeable atomic membranes from graphene sheets. *Nano Lett.* **8**, 2458–2462 (2008).
22. R. R. Nair, H. A. Wu, P. N. Jayaram, I. V. Grigorieva, A. K. Geim, Unimpeded permeation of water through helium-leak-tight graphene-based membranes. *Science* **335**, 442–444 (2012).
23. H. W. Kim, H. W. Yoon, S.-M. Yoon, B. M. Yoo, B. K. Ahn, Y. H. Cho, H. J. Shin, H. Yang, U. Paik, S. Kwon, J.-Y. Choi, H. B. Park, Selective gas transport through few-layered graphene and graphene oxide membranes. *Science* **342**, 91–95 (2013).
24. H. Li, Z. Song, X. Zhang, Y. Huang, S. Li, Y. Mao, H. J. Ploehn, Y. Bao, M. Yu, Ultrathin, molecular-sieving graphene oxide membranes for selective hydrogen separation. *Science* **342**, 95–98 (2013).
25. A. Akbari, P. Sheath, S. T. Martin, D. B. Shinde, M. Shaibani, P. C. Banerjee, R. Tkacz, D. Bhattacharyya, M. Majumder, Large-area graphene-based nanofiltration membranes by shear alignment of discotic nematic liquid crystals of graphene oxide. *Nat. Commun.* **7**, 10891 (2016).
26. Q. Yang, Y. Su, C. Chi, C. T. Cherian, K. Huang, V. G. Kravets, F. C. Wang, J. C. Zhang, A. Pratt, A. N. Grigorenko, F. Guinea, A. K. Geim, R. R. Nair, Ultrathin graphene-based membrane with precise molecular sieving and ultrafast solvent permeation. *Nat. Mater.* **16**, 1198–1202 (2017).
27. L. Nie, K. Goh, Y. Wang, J. Lee, Y. Huang, H. Enis Karahan, K. Zhou, M. D. Guiver, T.-H. Bae, Realizing small-flake graphene oxide membranes for ultrafast size-dependent organic solvent nanofiltration. *Sci. Adv.* **6**, eaaz9184 (2020).
28. B. Mi, Scaling up nanoporous graphene membranes. *Science* **364**, 1033–1034 (2019).
29. B. Liang, H. Wang, X. Shi, B. Shen, X. He, Z. A. Ghazi, N. A. Khan, H. Sin, A. M. Khattak, L. Li, Z. Tang, Microporous membranes comprising conjugated polymers with rigid backbones enable ultrafast organic-solvent nanofiltration. *Nat. Chem.* **10**, 961–967 (2018).
30. X. He, H. Sin, B. Laing, Z. A. Ghazi, A. M. Khattak, N. A. Khan, H. R. Alanagh, L. Li, X. Lu, Z. Tang, Controlling the selectivity of conjugated microporous polymer membrane for efficient organic solvent nanofiltration. *Adv. Funct. Mater.* **29**, 1900134 (2019).
31. S. Zhou, Y. Zhao, J. Zheng, S. Zhang, High-performance functionalized polymer of intrinsic microporosity (PIM) composite membranes with thin and stable interconnected layer for organic solvent nanofiltration. *J. Membr. Sci.* **591**, 117347 (2019).
32. Z. Zhou, X. Li, D. Guo, D. B. Shinde, D. Lu, L. Chen, X. Liu, L. Cao, A. M. Aboalsaud, Y. Hu, Z. Lai, Electropolymerization of robust conjugated microporous polymer membranes for rapid solvent transport and narrow molecular sieving. *Nat. Commun.* **11**, 5323 (2020).
33. Y. Li, J. Zhu, S. Li, Z. Guo, B. Van der Bruggen, Flexible aliphatic–aromatic polyamide thin film composite membrane for highly efficient organic solvent nanofiltration. *ACS Appl. Mater. Interfaces* **12**, 31962–31974 (2020).
34. D. Ren, Y. Li, S. Ren, T.-Y. Liu, X.-L. Wang, Microporous polyarylate membrane with nitrogen-containing heterocycles to enhance separation performance for organic solvent nanofiltration. *J. Membr. Sci.* **610**, 118295 (2020).

35. F. Alduraiei, S. Kumar, J. Liu, S. P. Nunes, G. Szekely, Rapid fabrication of fluorinated covalent organic polymer membranes for organic solvent nanofiltration. *J. Membr. Sci.* **648**, 120345 (2022).
36. D. B. Shinde, G. Sheng, X. Li, M. Ostwal, A.-H. Emwas, K.-W. Huang, Z. Lai, Crystalline 2D covalent organic framework membranes for high-flux organic solvent nanofiltration. *J. Am. Chem. Soc.* **140**, 14342–14349 (2018).
37. W. Zhang, L. Zhang, H. Zhao, B. Li, H. Ma, A two-dimensional cationic covalent organic framework membrane for selective molecular sieving. *J. Mater. Chem. A* **6**, 13331–13339 (2018).
38. J. Liu, G. Han, D. Zhao, K. Lu, J. Gao, T.-S. Chung, Self-standing and flexible covalent organic framework (COF) membranes for molecular separation. *Sci. Adv.* **6**, eabb1110 (2020).
39. D. B. Shinde, L. Cao, A. D. Dinga Wonanke, X. Li, S. Kumar, X. Liu, M. N. Hedhili, A.-H. Emwas, M. Addicoat, K.-W. Huang, Z. Lai, Pore engineering of ultrathin covalent organic framework membranes for organic solvent nanofiltration and molecular sieving. *Chem. Sci.* **11**, 5434–5440 (2020).
40. R. Shevate, D. L. Shaffer, Large-area 2D covalent organic framework membranes with tunable single-digit nanopores for predictable mass transport. *ACS Nano* **16**, 2407–2418 (2022).
41. N. A. A. Sani, W. J. Lau, A. F. Ismail, Polyphenylsulfone-based solvent resistant nanofiltration (SRNF) membrane incorporated with copper-1,3,5-benzenetricarboxylate (Cu-BTC) nanoparticles for methanol separation. *RSC Adv.* **5**, 13000–13010 (2015).
42. X. Cheng, X. Jinag, Y. Zhang, C. H. Lau, Z. Xie, D. Ng, S. J. D. Smith, M. R. Hill, L. Shao, Building additional passageways In polyamide membranes with hydrostable metal organic frameworks to recycle and remove organic solutes from various solvents. *ACS Appl. Mater. Interfaces* **9**, 38877–38886 (2017).
43. X. Guo, D. Liu, T. Han, H. Huang, Q. Yang, C. Zhong, Preparation of thin film nanocomposite membranes with surface modified MOF for high flux organic solvent nanofiltration. *AIChE J.* **63**, 1303–1312 (2017).
44. Y. Li, J. Li, R. B. Soria, A. Volodine, B. Van der Bruggen, Aramid nanofiber and modified ZIF-8 constructed porous nanocomposite membrane for organic solvent nanofiltration. *J. Membr. Sci.* **603**, 118002 (2020).
45. S. Wang, J. Liu, B. Pulido, Y. Li, D. Mahalingam, S. P. Nunes, Oriented zeolitic imidazolate framework (ZIF) nanocrystal films for molecular separation membranes. *ACS Appl. Nano Mater.* **3**, 3839–3846 (2020).
46. Y. Chen, Y. Bai, L. Meng, W. Zhang, J. Xia, Z. Xu, R. Sun, Y. Lv, T. Liu, Engineering nanocomposite metal-phenolic network membranes with hollow MOFs via in-situ etching for high-efficiency organic solvent nanofiltration. *Chem. Eng. J.* **437**, 135289 (2022).
47. X. Yu, W. Fan, V. Wee, D. Shi, H. Yuan, Y. Ying, Y. D. Yuan, Z. Yang, Y. Feng, D. Sun, D. Zhao, Polycrystalline iron(III) metal-organic framework membranes for organic solvent nanofiltration with high permeance. *J. Membr. Sci.* **644**, 120130 (2022).
48. J. E. Schmidt, C.-Y. Chen, S. K. Brand, S. I. Zones, M. E. Davis, Facile synthesis, characterization, and catalytic behavior of a large-pore zeolite with the IWV framework. *Chem. A Eur. J.* **22**, 4022–4029 (2016).
49. J. Wu, K. Zhang, H. Yoo, Y. Lee, In silico generation of a topologically diverse zeolite-templated carbon library. *Cryst. Growth Des.* **22**, 123–130 (2022).
50. J. P. Perdew, K. Burke, M. Ernzerhof, Generalized gradient approximation made simple. *Phys. Rev. Lett.* **77**, 3865–3868 (1996).
51. G. Kresse, M. Marsman, J. Furthmüller, *Vienna Ab-Initio Package Vienna Simulation: VASP the GUIDE. VASP Man.* (2014), 237 pp.
52. G. Kresse, D. Joubert, From ultrasoft pseudopotentials to the projector augmented-wave method. *Phys. Rev. B* **59**, 1758–1775 (1999).
53. P. E. Blöchl, Projector augmented-wave method. *Phys. Rev. B* **50**, 17953–17979 (1994).
54. K. Chenoweth, A. C. T. van Duin, W. A. Goddard, ReaxFF reactive force field for molecular dynamics simulations of hydrocarbon oxidation. *J. Phys. Chem. A* **112**, 1040–1053 (2008).
55. R. L. Martin, B. Smit, M. Haranczyk, Addressing challenges of identifying geometrically diverse sets of crystalline porous materials. *J. Chem. Inf. Model.* **52**, 308–318 (2012).
56. A. S. Michaels, Analysis and prediction of sieving curves for ultrafiltration membranes: A universal correlation? *Sep. Sci. Technol.* **15**, 1305–1322 (1980).
57. B. Van der Bruggen, J. Schaep, D. Wilms, C. Vandecasteele, A comparison of models to describe the maximal retention of organic molecules in nanofiltration. *Sep. Sci. Technol.* **35**, 169–182 (2000).
58. S. Singh, K. C. Khulbe, T. Matsuura, P. Ramamurthy, Membrane characterization by solute transport and atomic force microscopy. *J. Membr. Sci.* **142**, 111–127 (1998).
59. C. R. Wilke, P. Chang, Correlation of diffusion coefficients in dilute solutions. *AIChE J.* **1**, 264–270 (1955).
60. K. Miyabe, R. Isogai, Estimation of molecular diffusivity in liquid phase systems by the Wilke-Chang equation. *J. Chromatogr. A* **1218**, 6639–6645 (2011).
61. W. Schotte, Prediction of the molar volume at the normal boiling point. *Chem. Eng. J.* **48**, 167–172 (1992).

Acknowledgments

Funding: This work was supported by Samsung Research Funding and Incubation Center of Samsung Electronics (SRFC-MA1902-08) and Inha University Research Grant. **Author contributions:** Conceptualization: M.C. Methodology and investigation: C.K. (membrane preparation, membrane characterization, and separation performance), J.C. (separation performance), Y.L. (computational modeling), and H.S.C. (structural analysis). Funding acquisition: D.-Y.K. and M.C. Supervision: D.-Y.K. and M.C. Writing—original draft: C.K., D.-Y.K., Y.L., and M.C. **Competing interests:** The authors declare that they have no competing interests. **Data and materials availability:** All data needed to evaluate the conclusions in the paper are present in the paper and/or the Supplementary Materials.

Submitted 8 September 2022
Accepted 6 January 2023
Published 10 February 2023
10.1126/sciadv.ade7871

ScienceAdvances

Bottom-up synthesis of two-dimensional carbon with vertically aligned ordered micropores for ultrafast nanofiltration

Chaehoon Kim, Dong-Yeun Koh, Yongjin Lee, Jihoon Choi, Hae Sung Cho, and Minkee Choi

Sci. Adv., **9** (6), eade7871.
DOI: 10.1126/sciadv.ade7871

Science Advances (ISSN) is published by the American Association for the Advancement of Science. 1200 New York Avenue NW, Washington, DC 20005. The title *Science Advances* is a registered trademark of AAAS.